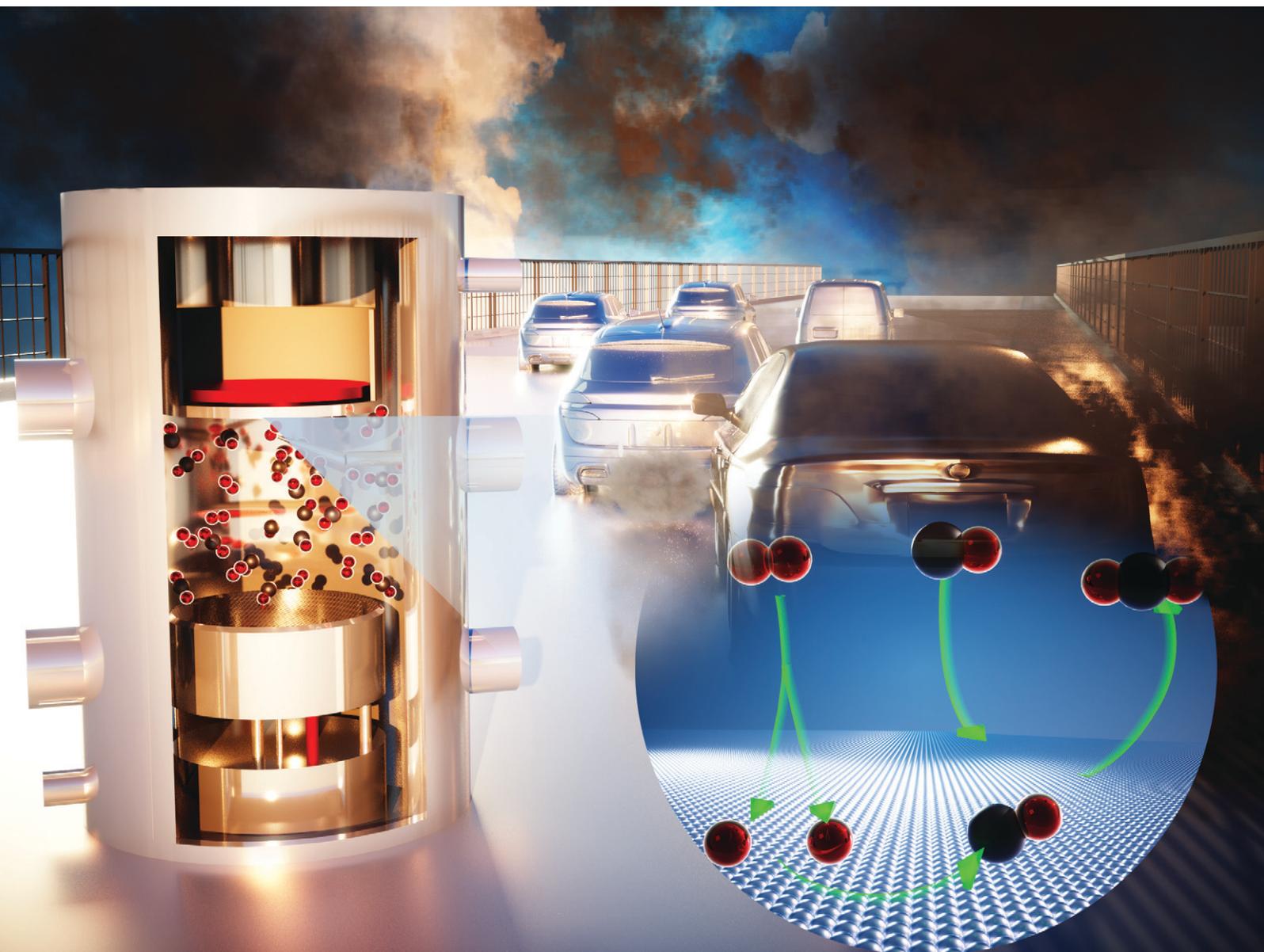# Reaction Chemistry & Engineering

Linking fundamental chemistry and engineering to create scalable, efficient processes

ROYAL SOCIETY
OF CHEMISTRY

PAPER
Nawaf M. Alghamdi *et al.*
Low-temperature CO oxidation over Rh/Al$_2$O$_3$ in a
stagnation-flow reactor

PAPER

Check for updates

Low-temperature CO oxidation over Rh/Al$_2$O$_3$ in a stagnation-flow reactor†

Nawaf M. Alghamdi, [iD] *[a] Ribhu Gautam, [iD] [a] Jorge Gascon, [iD] [b] Dionisios G. Vlachos [iD] [cd] and S. Mani Sarathy [iD] [a]

Anthropogenic activities are responsible for nearly half of the total CO emissions in the US. A significant amount of CO is emitted by the transportation sector. Three-way catalytic converters are widely employed to treat CO emissions from gasoline engines; however, current kinetic mechanisms for CO oxidation and the water-gas shift (WGS) reaction on Rh are limited and were built based on data collected over a narrow range of conditions. To fill in this gap, we conducted low-temperature CO oxidation and WGS experiments on 5 wt% Rh/Al$_2$O$_3$ in a stagnation-flow reactor, which allows for reducing the problem to one dimension and simplifies the development of accurate kinetic models. We characterized the catalyst *via* N$_2$-physisorption, ICP, XRD, H$_2$-chemisorption, H$_2$-TPR, STEM and EELS. We studied the effects of pressure, temperature, flowrate, and the presence of H$_2$O on the conversion of CO to CO$_2$ and on the WGS reaction over the temperature range relevant to aftertreatment systems. The total operating pressure affected the resolution of the experimental measurements. Higher temperatures resulted in higher CO$_2$ production due to faster kinetics. Investigating the reaction order with respect to O$_2$ showed three distinct kinetic regimes, where the order is positive below the stoichiometric ratio, beyond which a negative order was observed which decreased with increasing O$_2$ content. With respect to CO, the order was positive below the stoichiometric ratio, beyond which the order was negative. When increasing and reducing the O$_2$ content, we observed bistability manifested as a hysteresis behavior, which is attributed to the oxidation (by O$_2$) and reduction (by CO) of the metal. This thorough experimental study aids in developing accurate and versatile CO oxidation on Rh kinetic mechanisms that predict reactivity over a wide range of conditions.

^{a} *Clean Combustion Research Center, King Abdullah University of Science and Technology (KAUST), Thuwal, 23955 Saudi Arabia.*
E-mail: nawaf.alghamdi@kaust.edu.sa
^{b} *KAUST Catalysis Center, King Abdullah University of Science and Technology (KAUST), Thuwal, 23955 Saudi Arabia*
^{c} *Department of Chemical and Biomolecular Engineering, University of Delaware, 150 Academy Street, Newark, DE, 19716 USA*
^{d} *Catalysis Center for Energy Innovation, RAPID Manufacturing Institute, Delaware Energy Institute (DEI), 221 Academy Street, Newark, DE, 19716 USA*
† Electronic supplementary information (ESI) available. See DOI: https://doi.org/10.1039/d2re00235c

Introduction

According to the United Nations, air pollution causes the premature death of nearly 7 million people, including 600 000 children, every year.[1] One of the six criteria pollutants responsible for air pollution is carbon monoxide (CO). In the US, the transport sector alone produces 44% of CO emissions.[2] Moreover, up to 95% of all CO emissions in US cities are due to motor vehicle exhaust.[3] Even though electrification of passenger vehicles seems to be promising from an economic point of view, it faces many non-economic

barriers especially in emerging markets and developing countries, where there is a heavy reliance on second-hand markets, an absence of governmental environmental pledges, and a severe lack of cheap and fast charging infrastructure.[4] Therefore, a pragmatic and more immediate way of reducing the current emissions resulting from the 1 billion passenger vehicles on the road today is to improve the current aftertreatment systems.

Noble metals have been used as catalysts for the oxidation of CO, as they show high stability and excellent performance with various supports and dopants.[5] Feng *et al.*[5] comprehensively reviewed CO oxidation performance and reaction mechanisms on platinum (Pt), gold (Au), palladium (Pd), silver (Ag), ruthenium (Ru), rhodium (Rh), and iridium (Ir), and highlighted the need for developing noble metal catalysts that are active for CO oxidation over the range of 100–250 °C. In a review of CO oxidation on Rh and Ru, Dey *et al.*[6] stated that Rh and Ru-based catalysts are the most effective for CO oxidation at low temperatures.

In the context of passenger vehicle aftertreatment, three-way catalysts are implemented in gasoline-engine vehicles to simultaneously remove carbon monoxide (CO), nitric oxide

(NO), and unburned hydrocarbons (UHC). Of particular interest are the CO emissions because they constitute up to 1 wt% of the exhaust emissions.[7] The three-way catalyst technology relies on a combination of platinum (Pt) and rhodium (Rh) noble metals as the active sites, supported on alumina (Al_2O_3) for high surface area and on cerium oxides for oxygen storage.[7,8] On the surface of the three-way catalyst, CO is oxidized by O_2 to CO_2 (eqn 1). This reaction has been extensively studied, especially on Pt, which is an excellent oxidation catalyst (see ref. 9–14). In the presence of H_2O, such as in aftertreatment systems, the water-gas shift (WGS) reaction becomes important (eqn 2).

$$2CO + O_2 \rightarrow 2CO_2 \qquad (1)$$

$$CO + H_2O \rightarrow H_2 + CO_2 \qquad (2)$$

CO oxidation on Rh has also been studied (see ref. 15–21) but to a lesser extent, with limited literature in regard to the development of microkinetic mechanisms. Table 1 is a comparative summary of some microkinetics studies of CO oxidation over Rh/Al_2O_3. Maestri *et al.*[22] generated a kinetic mechanism for methane chemistry on Rh, which was a modification to an earlier mechanism by Mhadeshwar and Vlachos.[23] The mechanism showed good agreement with experimental data obtained from an annular reactor. However, the focus of this mechanism was methane chemistry, not CO oxidation or the WGS reaction. More specifically to CO, Karakaya *et al.*[19,24] generated a mechanism for CO oxidation on Rh in a stagnation-flow reactor, and the mechanism was validated using packed bed reactor measurements in the range of 27 to 250 °C. However, the Karakaya stagnation-flow reactor data[19,24] were obtained at higher temperatures, namely 250, 400 and 600 °C, with a fixed inlet composition at each temperature. More recently, Shimokuri *et al.*[18] generated a mechanism for CO oxidation on Rh based on a combination of two experiments: a honeycomb catalyst for detecting gaseous species, and a powder catalyst for detecting surface species *via* in situ FTIR measurements. They coupled those experiments with new insights from characterization data; namely, Shimokuri *et al.* reported that CO adsorbed on Rh in a twin fashion, *i.e.*, two CO molecules adsorbed on one Rh site which then reacted with a neighboring adsorbed oxygen to create CO_2. This was an additional pathway they included in the mechanism.[18] However, Shumokuri *et al.*[18] tested a fixed

stoichiometric inlet composition and detected reactivity only starting at 220 °C.

Accurate kinetic data can be obtained *via* a variety of reactors, such as the annular reactor used by Maestri *et al.*[22] and the honeycomb monolith used by Shumokuri *et al.*[18] However, for a large number of species, assumptions are often made to simplify reactor modeling and reduce the computational time, which can result in uncertainties. An attractive alternative is to utilize reactors whose flow-fields are established and easy to model, such as channel and stagnation flows.[25] These reactors allow for testing kinetic models under well-defined near-surface convective-diffusive transport conditions, which may be difficult to establish in configurations where access to the catalyst surface, such as in a plug-flow reactor, is not possible.[26] The stagnation flow reactor concept is particularly useful in kinetic studies because it can be modeled as a boundary layer problem described by a set of ordinary differential equations.[27] The boundary layer is adjacent to the catalyst surface where the concentration is uniform in the radial direction and only changes in the axial/vertical direction away from the surface.[27] This simplifies the numerical simulations of the reactor, whose flow field is 2D, to a 1D problem.[25] These attributes of the stagnation-flow reactor have led many groups to utilize it.[28–30]

There are no studies on CO oxidation and the WGS reaction on Rh in a stagnation-flow reactor in the low temperature regime typical of vehicle aftertreatment systems. As the existing literature experimental data are in a narrow range from either a temperature, flowrate or inlet composition perspectives, the mechanisms generated tend to be applicable to a narrow range of conditions. Therefore, the aim of this study is to obtain a better understanding of the direct oxidation of CO and the WGS reaction on 5 wt% Rh/Al_2O_3 using a stagnation-flow reactor at temperatures relevant to aftertreatment systems (175 to 275 °C). The reason behind choosing 5 wt% was to mimic the catalyst of Karakaya *et al.*;[19,24] however, the results may be applicable to other metal loadings since CO oxidation on Rh/Al_2O_3 is independent of metal loading.[31] This thorough, low-temperature study includes the effects of temperature, flowrate, pressure, inlet composition, and the addition of H_2O. The combination of the various experimental conditions as well as the nature of the one-dimensional reactor paves the way for accurate kinetic modeling of low-temperature CO oxidation and the WGS reaction in the future.

Table 1 A summary of some microkinetic studies of CO oxidation over Rh/Al_2O_3

	Karakaya *et al.*[19,24]	Shumokuri *et al.*[18]	Maestri *et al.*[22]
Reactor configuration	Stagnation-flow	Honeycomb + FTIR	Annular reactor
Temperature (°C)	250, 400, and 600	150 to 325	350 to 920
Pressure (bar)	0.5	—	1
Rh metal loading	5 wt% Rh	0.7 g L^{-1}	4 wt%
Dispersion (%)	1.2	97	70
Inlet gases	CO, O_2, Ar	CO, O_2, N_2	N_2, O_2, CH_4, CO, H_2O, CO_2, H_2
Inlet composition	Fixed at each temperature	Stoichiometric	Multiple conditions

Methodology

Catalyst preparation

The catalyst is 5 wt% Rh/Al_2O_3, purchased from Sigma-Aldrich (article number 212857). 200 mg of the catalyst powder was dispersed in 12 mL of DI water. The mixture was stirred at 1000 rpm and 40 °C for 12 hours. The resulting slurry was coated on an α-Al_2O_3 ceramic crucible. The coating was done using a spin coater (specialty coating systems G3P-8) with a heating element (120 °C, 1000 RPM), which has the advantage of creating homogeneous and thin coating layers on surfaces, beneficial for minimizing diffusion effects. Before coating, we treated the crucible surface with plasma to increase its hydrophilicity, which in turn increased the wettability (and therefore the coating quality) of the surface. After coating the catalyst, the crucible was calcined in air at 700 °C for 2 hours (as implemented in the literature[19,24]) then finally loaded into the reactor.

Characterization of the catalyst powder

We characterized the catalyst powder *via* N_2-physisorption, inductively coupled plasma optical emission spectroscopy (ICP-OES), X-ray diffraction (XRD), temperature-programmed reduction (TPR), H_2-chemisorption, scanning transmission electron microscopy (STEM), and electron energy loss spectroscopy (EELS).

The N_2-physisorption test was conducted at 77 K on a Micromeritics ASAP 2420 with around 50 mg of the catalyst powder after calcination in air at 700 °C for 2 hours and applying vacuum overnight. The surface area was estimated by the Brunauer–Emmett–Teller (BET) method in a relative pressure range of 0.05–0.25. The pore volume was determined by the Barrett–Joyner–Halenda (BJH) method (desorption branch).

To determine the exact wt% of the Rh metal and confirm the specifications of the catalyst, we conducted experiments in 5110 ICP-OES (Agilent Technologies). First, the catalyst was digested in *aqua regia* (a mixture of nitric acid and hydrochloric acid with a 1:3 molar ratio). Around 10 mg of the catalyst and 8 mL of *aqua regia* was loaded into Polytetrafluoroethylene (PTFE) vessels. The sample solution was digested at 220 °C for 20 minutes in an ETHOS 1 closed vessel microwave-assisted digestion instrument. After cooling to room temperature, the sample was diluted in deionized water and then tested *via* ICP-OES.

To determine the crystallinity of the catalyst support, we conducted XRD experiments on the catalyst powder before and after calcination (in air at 700 °C for 2 hours) using a Bruker XRD D8 ADVANCE instrument in the Bragg–Brentano configuration using CuK_α radiation and an EIGER2 R detector. The step size was 0.02° and the 2θ range was 10–90°. The Joint Committee on Powder Diffraction Standards (JCPDS) cards were used to identify the crystalline phase of the catalyst support.

To determine the reducibility of the catalysts, H_2-temperature programmed reduction (H_2-TPR) experiments were performed in a Micromeretics AutoChem 2950 HP instrument. About 200 mg of the calcined catalyst was packed into a quartz tube. To degas the powder, the catalyst was purged by high purity helium at 50 mL min^{-1} and 120 °C for one hour then cooled to room temperature. The sample was heated to 800 °C at a rate of 10 °C min^{-1} under 10% H_2/Ar flow of 50 mL min^{-1}. A thermal conductivity detector (TCD) was used to monitor the consumption of hydrogen. An H_2/Rh ratio of 2:1 was used (*i.e.* H_2 adsorbs dissociatively, where one H atom adsorbs to one Rh site).[32,33]

Static H_2-chemisorption measurements were performed at 34 °C using a Micromeritics ASAP 2020 instrument. Around 100 mg of the catalyst (calcined in air at 700 °C for 2 hours) was reduced *in situ* under H_2 flow for one hour at 300 °C (the same reduction temperature used in the experiment), evacuated at that temperature for 3 hours, and then cooled to 34 °C. A total chemisorption profile was obtained from 100 to 450 mmHg in increments of 50 mmHg. The sample was degassed for a few hours to remove the physisorbed amount of H_2, then another chemisorption profile was obtained (over the same pressure range) to capture the amount of physisorbed H_2. The difference between the two isotherms corresponded to the chemisorbed H_2. By extrapolating the chemisorbed H_2 isotherm to zero pressure, we determined the hydrogen uptake and therefore the catalyst dispersion and average particle size.

STEM images of the reduced catalyst were obtained using Titan Themis Z (Thermo-Fisher Scientific) to examine the catalyst morphology and quantify the particle size distribution. The analysis was performed by operating the microscope at an acceleration voltage of 300 kV. Prior to STEM imaging, the powder catalyst was loaded in a packed bed reactor and reduced by heating the catalyst to 300 °C (the same reduction temperature used in the experiment) at a rate of 10 °C min^{-1} and flowing H_2 (8 mL min^{-1}) for 1 hour. After reduction, the reactor was cooled with helium, then sealed and moved into a glovebox. In the glovebox, where the O_2 and H_2O concentrations were lower than 1 ppm, the reduced catalyst was mixed with isopropanol, and a small amount of the solution was drop-casted onto a carbon-coated copper TEM grid. The grid was placed in a TEM vacuum transfer holder to avoid exposure to air outside the glovebox. Bright-field (BF) and high-angle annular dark field (HAADF) images were obtained while simultaneously generating elemental maps using EELS. In addition, EELS line scan analysis was performed to ensure the absence of RhO_x and therefore confirm the success of the catalyst reduction and accuracy of the particle size distribution.

Stagnation-flow reactor design

The experiments were conducted in a stagnation-flow reactor (depicted in Fig. 1), which allows to numerically model the system as a one-dimensional reacting flow, enabling accurate kinetic modeling and a coupling of gas and surface phase chemistry effects.[27] Reactant species were
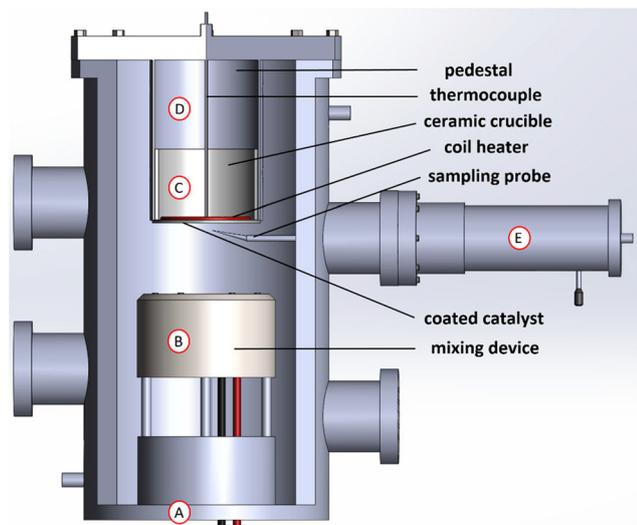
Fig. 1 Schematic depiction of the stagnation-flow reactor: "A" is the bottom of the reactor where the inlet gases were flowed upwards, "B" is for mixing the inlet gases, "C" is the ceramic crucible on which Rh/Al_2O_3 was coated, "D" is the pedestal holding the crucible in place, and "E" is the sampling probe manual step manipulator.

flowed from gas cylinders using MKS mass-flow controllers towards the bottom of the reactor chamber (shown as "A" in Fig. 1). The chamber was oriented vertically for zero buoyancy effects and the chamber pressure was measured by an MKS baratron transducer. Reactant species were then perfectly mixed inside the chamber *via* a mixing device (shown as "B" in Fig. 1), whose design is based on that of a McKenna burner.[34] Reactant species flowed upwards towards the catalyst coated onto a heated ceramic stagnation plate made of α-Al_2O_3 ("C" in Fig. 1) and held in place *via* a pedestal ("D" in Fig. 1).

The plate was heated by a coil heater (purchased from Micropyretics Heaters International), controlled by a feedback loop based on measurements from a type-K thermocouple placed right above the coil. The temperature of the catalyst surface was measured using another type-K thermocouple placed directly on the catalyst surface (*i.e.* the bottom of the stagnation plate), whereby the thermocouple was subjected to the same flow conditions to which the catalyst surface was subjected, especially the cooling effect due to the high flowrates involved. The thermocouple was ensured to be placed immediately on the surface by visual inspection through an observation window mounted on the chamber.

Probe-based sampling was used to measure gaseous reactant and stable product species concentrations as a function of distance from the catalyst surface. A probe with an outer diameter of 250 μm was used and placed slightly off-center, to minimize the probe disturbance of the flow. The probe was moved up and down *via* a step manipulator (shown as "E" in Fig. 1, purchased from CHI-VAC), which was mounted on the chamber from the outside and operated manually. The probe was ensured to be placed at the catalyst surface for distance-zero measurements by visual inspection.

The steady-state conversion of CO to CO_2 (and production of H_2 in the case of the water-gas shift reaction experiments) was measured directly using gas chromatography (GC). The GC used was the Agilent Refinery Gas Analysis system (7890 A), following the ASTM D1945 and D1946 methods. One TCD was used to detect O_2, N_2, CO, and CO_2 (for CO oxidation), and another TCD to detect H_2 (for WGS). The GC was calibrated using a standard calibration gas. In addition to the sampling line, another output of the chamber was towards the exhaust, where a suction pump (Varian, model DS 302) was installed.

To add H_2O to the feed, a nebulizer (purchased from Precision Glassblowing) was used to vaporize the H_2O as part of a vaporization chamber (design taken from ref. 35). The water was fed to the nebulizer *via* a syringe pump (purchased from New Era Pump Systems). The vaporization chamber as well as the tubing which fed the vapor to the system were heated to 120 °C to prevent condensation. To ensure that the vapor would not condense upon mixing with the feed CO, O_2, and N_2 gases, the entire gaseous reactant feed needed to be heated. An in-line heater (purchased from Kanthal) was used to heat the gaseous reactant species to 165 °C before mixing with the vapor. All the feedlines were insulated to minimize heat losses before entering the reactor, at which point the temperature was measured using a type-K thermocouple. Additionally, an H_2O adsorption column (clean gas moisture filter, purchased from Agilent) was installed downstream the reactor sampling port to prevent H_2O from entering the GC. Lastly, given that the Varian suction pump has a limited temperature rating of 40 °C, the exhaust line of the reactor chamber was cooled to 20 °C using a chiller (purchased from Julabo) before entering the pump.

Testing procedure and reaction conditions

Before conducting CO oxidation experiments, a deactivation test was performed, where CO_2 production at a fixed distance (zero), fixed surface temperature (275 °C), and fixed CO : O_2 molar ratio (2 : 1) was measured as a function of time for over five hours. The point in time at which the production of CO_2 started decreasing was deemed the deactivation time, which was the maximum operating time for the experiments. Henceforward, whenever the deactivation time was approached, the catalyst was regenerated *in situ* by oxidation at 300 °C for 30 minutes under 10% O_2/N_2 flow then reduction at 300 °C for 30 minutes under 10% H_2/N_2 flow. In addition to testing for deactivation, initial experiments were performed to quantify the relative error of the gas chromatograph.

Table 2 summarizes the experimental conditions. Three pressures (300, 500 and 700 mbar) were tested to investigate the effect of pressure on the resolution of the CO profile as a function of distance from the catalyst surface. This was done at 24 g min^{-1} and 275 °C under lean conditions. Two flowrates were tested to examine the effect of residence time: 24 g min^{-1} (corresponding to 0.6 bar and 20 SLM of

2500 | *React. Chem. Eng.*, 2022, **7**, 2497–2507

This journal is © The Royal Society of Chemistry 2022

Table 2 Summary of the experimental conditions. The total flowrate is shown in g/min because in experiments where H_2O was added as liquid to be vaporized, it was only possible to determine the flowrate based on mass

Procedure	Flowrate (g min^{-1})	CO:O$_2$ ratio	N$_2$ content (SLM)	Temperature (°C)	H$_2$O content (mol%)	Total pressure (bar)
Deactivation	24	2:1	18	275	0	0.6
Effect of pressure	24	1:1	18	275	0	0.3, 0.5, 0.7
CO oxidation	24		18 & 19		0	0.6
	35	2:1 & 1:1	27 & 28	175, 200, 225, 250, 275	0	0.8
	35		27 & 28		1.0	0.8
	35		27 & 28		1.7	0.8
Reaction Order & Hysteresis		O$_2$:CO = 0.4 to 4.0	14 to 18	300		
	24	CO:O$_2$ = 0.4 to 4.0	14 to 18	300	0	0.6
		1:1	17	200, 225, 250, 275		
Water-gas shift	35	CO:H$_2$O = 1:1	30	275	1.7	0.8

dry gas total flow) and 35 g min^{-1} (corresponding to 0.8 bar and 30 SLM of dry gas total flow). At each flowrate, two inlet compositions were tested: stoichiometric (CO:O$_2$ = 2:1), and lean (CO:O$_2$ = 1:1), with N$_2$ as the balance gas. At each inlet composition, reactivity profiles as a function of distance away from the catalyst surface were obtained from catalyst temperature of 175 to 275 °C in increments of 25 °C. From each reactivity profile, the conversion of CO was calculated as shown in eqn (3). After collecting reactivity profiles over the temperature range under one inlet composition, the catalyst was regenerated as stated above, before testing another inlet composition over the temperature range again.

$$\text{CO conversion (\%)} = \frac{\text{CO mol\% at the inlet} - \text{CO mol\% at the catalyst surface}}{\text{CO mol\% at the inlet}} \times 100 \qquad (3)$$

Additionally, reaction orders and hysteresis behavior were investigated by: (1) changing the O$_2$ inlet composition at the expense of the inert (N$_2$, see Table 2) from an O$_2$:CO ratio of 0.4 to 4 and then back to 0.4 while the temperature was fixed at 300 °C, (2) changing the CO inlet composition at the expense of the inert (N$_2$, see Table 2) from a CO:O$_2$ ratio of 0.4 to 4 and then back to 0.4 while the temperature was fixed at 300 °C, and (3) testing a fixed, lean inlet composition at four temperatures from 200 °C to 300 °C and then back to 200 °C.

To test for the effect of H$_2$O on CO oxidation at low temperature, reactivity profiles were obtained for stoichiometric and lean inlet compositions in the presence of 1 mol% and 1.7 mol% of H$_2$O over the temperature range and at a total flow of 35 g min^{-1}. Lastly, the water-gas shift reaction (eqn (2)) was tested by feeding 1.7 mol% of H$_2$O and 1.7 mol% of CO at 275 °C and 35 g min^{-1} of total flow.

Results and discussion

Catalyst characterization results

The BET area of the Rh/Al$_2$O$_3$ catalyst is 116 m^2 g^{-1} and the BJH pore volume is 0.50 cm^3 g^{-1}, which are typical values are for Al$_2$O$_3$-supported Rh.[36–40] The N$_2$-physisorption isotherm

is type IV and is attached in the ESI† (Fig. S1) The ICP results confirm that the metal content is approximately 5 wt%. The XRD results shed some light on the effect of calcining the catalyst in air at 700 °C for 2 hours. More specifically, as the catalyst was heated, the alumina support partially transitioned from the γ phase to the δ phase, which is the expected next phase in the well-established γ → δ → Θ → α sequence.[41] The XRD patterns of the as-purchased and calcined catalysts are shown in Fig. S2.† Given that the γ phase was still present after calcination, not much reduction in surface area was expected, which is confirmed by the fact that we attained similar physisorption results to those in the literature for Rh/Al$_2$O$_3$.[36–40]

Fig. S3† shows the H$_2$-TPR profile of the calcined Rh/Al$_2$O$_3$ catalyst. A broad peak with two shoulders can be observed: a first main shoulder near 160 °C along with a second one near 500 °C. This is attributed to the reduction of surface Rh (160 °C)[42–45] and Rh strongly interacting with Al$_2$O$_3$. Indeed, Burch et al.[46] studied the effect of calcination temperature on TPR of Rh/Al$_2$O$_3$. They show that the higher the calcination temperature, the later the TPR peak appeared and the broader the peak became. More specifically, when they calcined Rh/Al$_2$O$_3$ at 700 °C, they observed a broad peak in the range of 350–500 °C similar to the one shown in Fig. S3.† Additionally, the reduced catalyst H$_2$-chemisorption results show that the dispersion is 20% and the active particle diameter is 5.4 nm. This corroborates the STEM particle diameter of 5.1 nm, averaged from diameter measurements of over 100 particles from a few STEM images (distribution shown in Fig. 2(c)). The H$_2$-chemisorption profiles as a function of pressure are shown in Fig. S4.†

Low magnification bright field and high magnification dark field STEM images are shown in Fig. 2(a and b). The EELS images of the reduced catalyst are shown in Fig. 3; (a) is the raw HAADF image; (b), (c), and (d) highlight Al, O, Rh, respectively, and (e) shows the metal and the support
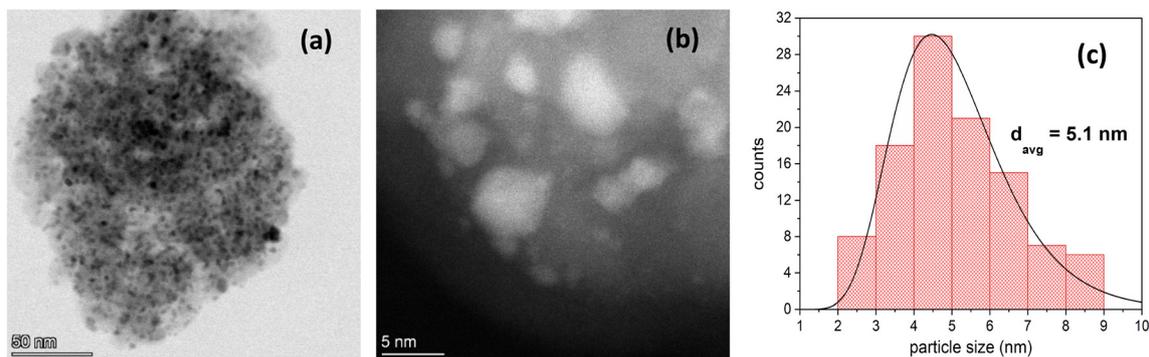
This journal is © The Royal Society of Chemistry 2022

React. Chem. Eng., 2022, 7, 2497–2507 | **2501**

Fig. 2 Bright (a) and dark (b) field STEM images of the reduced Rh/Al_2O_3 along with (c) the particle size distribution attained from measuring over 100 particles, with a log-normal distribution fit and average diameter of 5.1 nm.
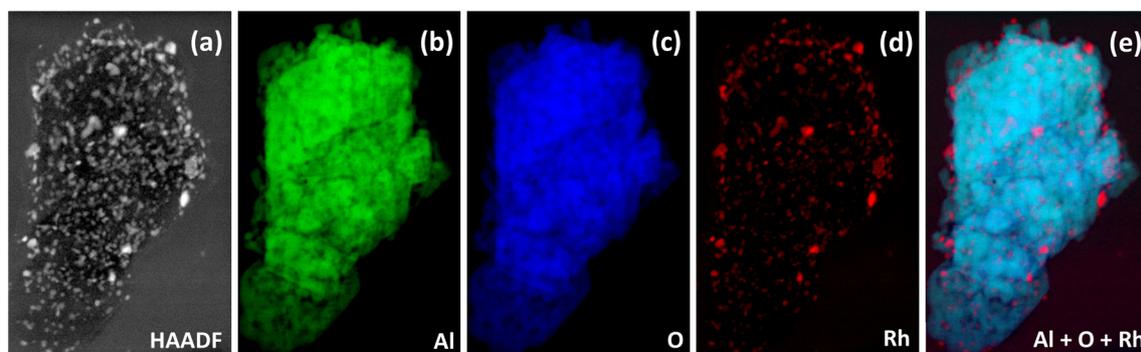

Fig. 3 EELS images of the reduced catalyst: (a) raw HAADF image on which EELS was performed, (b) Al alone, (c) O alone, (d) Rh alone, and (e) the combination of Al, O and Rh.

together. Fig. 4 shows the EELS line scan analysis (a) and the HAADF image on which the scan line analysis was performed (b and c). Fig. 4(a) shows that, prior to STEM imaging, the catalyst was successfully reduced. More specifically, the line scan analysis shows that Rh is present on the surface of AlO_x; however, while there is an O signal, it is significantly reduced when the Rh signal increases, excluding the possibility of the presence of RhO_x.

Deactivation results

We collected CO_2 production data as a function of time to determine the point at which the catalyst deactivated, which was set as the maximum for our experimental time window. For a conservative estimate, this was done at the highest experimental temperature (275 °C), the most reactive inlet composition (stoichiometric), and the highest residence time (total flow of 24 g min^{-1}). The results are shown in Fig. S5.† After oxidizing and reducing the catalyst, the oxidation of CO to CO_2 showed consistent results for nearly 3.5 hours. Therefore, whenever we performed experiments, we would regenerate the catalyst when we reached 3 hours of testing or when we finished a set of temperatures at the same inlet composition, whichever came first. Upon regenerating the catalyst, the same deactivation behavior was observed at roughly 3.5 hours as well. Lastly, measurements of the

reactive system repeatedly showed an error of less than 0.5% in conversion values. This demonstrated the regenerability of the catalyst.

Effects of pressure, residence time, temperature, and inlet composition on CO oxidation

The pressure played a role when optimizing the reactor to attain well-resolved species profiles of the reactive system. On the catalyst surface, CO_2 is produced from the oxidation of CO by O_2. CO_2 diffuses back towards the inlet, making it possible to detect a decreasing CO_2 mole fraction and increasing O_2 and CO mole fractions as the sampling probe is moved away from the catalyst surface towards the inlet (Fig. 6 and 7 are examples of this). Fig. 5 shows the effect of pressure on the resolution of the CO profile as a function of distance from the catalyst surface. The CO conversion remained the same at all pressures tested, but at a pressure of 700 mbar, the CO mole percentage reached the inlet composition 16 mm away from the catalyst surface. At 500 mbar, the distance was reduced to 12 mm. At 300 mbar, the distance was further reduced to 8 mm. This is explained by the fact that reducing the pressure results in increasing the inlet velocity. However, the sampling gas flowrate at 300 mbar was significantly reduced such that it would take a prohibitively long time to collect samples. So, high pressures

2502 | *React. Chem. Eng.*, 2022, **7**, 2497–2507

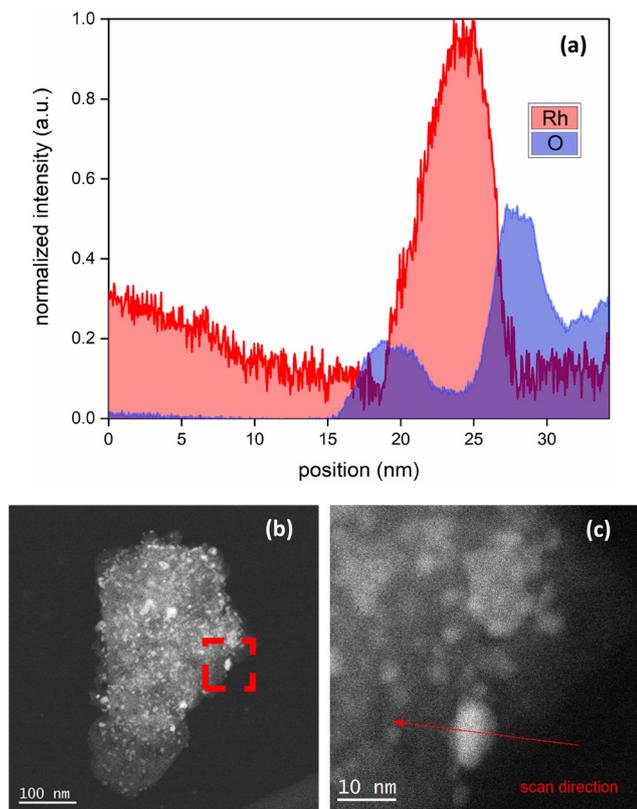This journal is © The Royal Society of Chemistry 2022

Fig. 4 (a) EELS line scan analysis, with (b) the low-magnification raw HAADF image chosen for the analysis and (c) a zoomed-in version of (b) on which the analysis was performed and the scan direction is shown.
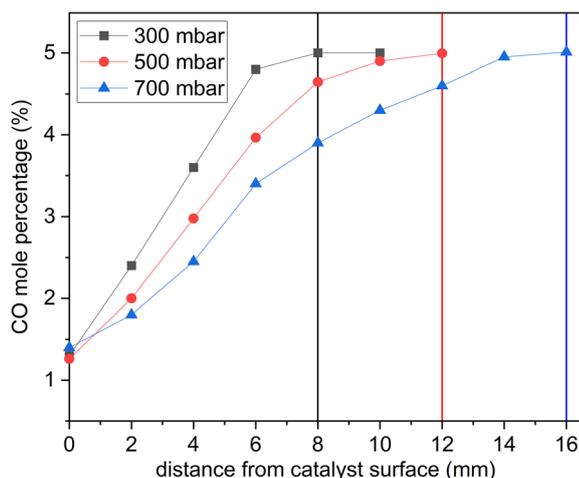

Fig. 5 CO mol% as a function of pressure at 24 g min^{-1} of total flow, 275 °C, and 5 mol% inlet of CO. The vertical lines show where the CO mol% reaches inlet composition levels (5 mol%) away from the catalyst surface. The experimental data points are connected by lines for ease of presentation.

cause species profiles to be resolved at a further distance from the surface, while low pressures hinder species detection.

To demonstrate the effect of residence time, Fig. 6 shows sample species profiles at 250 °C and a stoichiometric inlet composition under 24 and 35 g min^{-1} of total flow. The

production of CO_2 was higher at 24 g min^{-1}, which led the CO_2 diffusion distance back towards the feed to be longer. Specifically, the CO_2 mole percentage at 24 g min^{-1} reached nearly 5.5%, but at 35 g min^{-1}, it was only 2.5%. Additionally, the CO_2 mole percentage reached near-zero levels 10 mm away from the catalyst surface at 24 g min^{-1}, but it did so earlier, at 8 mm, under a total flow of 35 g min^{-1}.

To demonstrate the effect of temperature, Fig. 7 shows sample species profiles at a lean inlet composition under 35 g min^{-1} at 275 °C and 225 °C. The production of CO_2 was higher at higher temperatures: nearly 4% at 275 °C as opposed to 1.5% at 225 °C. The higher CO_2 production led the CO_2 mole percentage to reach near-zero levels at 8 mm at 275 °C, whereas it did so at 6 mm at 225 °C.

Table 3 shows the effects of residence time, inlet composition, and temperature on the CO conversion under all conditions tested. First, at the same inlet composition and temperature, the CO conversion levels were always higher at the lower flowrate. The higher reactivity is due to the higher residence time. Second, at the same flowrate and inlet composition, the reactivity increased as the temperature increased, which is due to higher reaction rates at higher temperatures.

As for the effect of inlet composition, the stoichiometric ratio was favored at the lower flowrate (24 g min^{-1}), but the lean ratio was slightly favored at the higher flowrate (35 g min^{-1}). Under the low flowrate and lean inlet composition, there was an abundance of O_2 that adsorbed on the surface and occupied more active sites at the expense of CO, which reduced the reactivity. Under the low flowrate and stoichiometric inlet composition, there was little competition on active sites, which resulted in higher conversion levels at the stoichiometric composition. The fact that we observed higher reactivity at the stoichiometric conditions agrees with findings by Gopinath et al.,[47] who reported maximum CO oxidation levels at the stoichiometric inlet ratio of CO and O_2 near 230 °C.

At the higher flowrate (35 g min^{-1}), the trend was reversed: lean conditions showed higher reactivity at temperatures below 250 °C. This agrees with findings by Bunluesin et al.,[16] who studied CO oxidation on Rh/Al_2O_3 and Rh/CeO_2 and observed that the adsorption of O_2 was rate limiting on the Al_2O_3 support. Campbell and White[48] reported that the adsorption and desorption reactions of O_2 and CO on Rh can be highly temperature dependent. They showed that at low temperatures, the rate of CO adsorption is high and inhibits the adsorption of O_2, leading to lower CO_2 production. More specifically, they reported that CO starts desorbing at 257 °C, allowing for more O_2 to adsorb. As the temperature increases, the inhibitive effect of CO coverage decreases, eventually becoming negligible near 275 °C.[48] So, at 35 g min^{-1} and below 250 °C, where CO coverage is significant, more O_2 in the inlet resulted in higher adsorption of O_2 and therefore higher CO conversion levels compared to the stoichiometric inlet composition. Additionally, the likelihood of adsorption can be quantified in the form of a sticking coefficient, which represents the probability (ranging from 0 to 1) for a certain molecule to adsorb on the surface. In
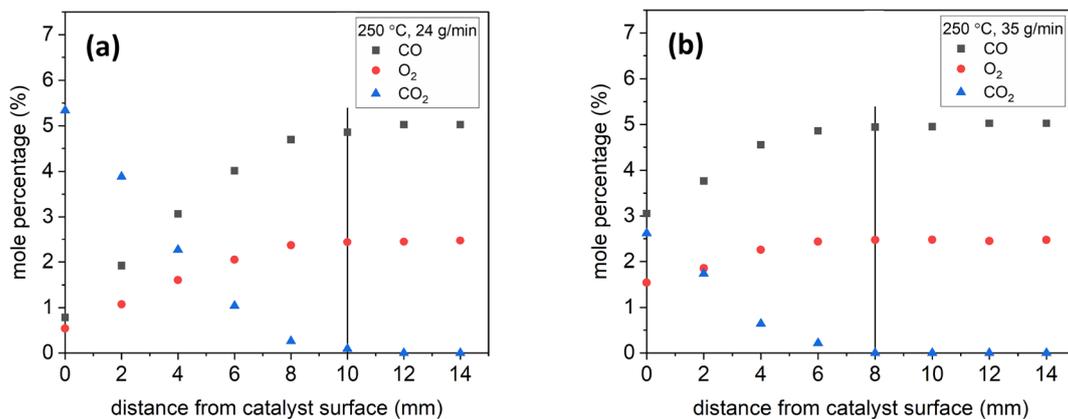
This journal is © The Royal Society of Chemistry 2022

React. Chem. Eng., 2022, 7, 2497–2507 | 2503

Fig. 6 Species profiles as a function of distance at 250 °C, stoichiometric inlet composition, and (a) 24 & (b) 35 g min^{-1}. The vertical lines show where the CO_2 near-zero levels were reached away from the surface.
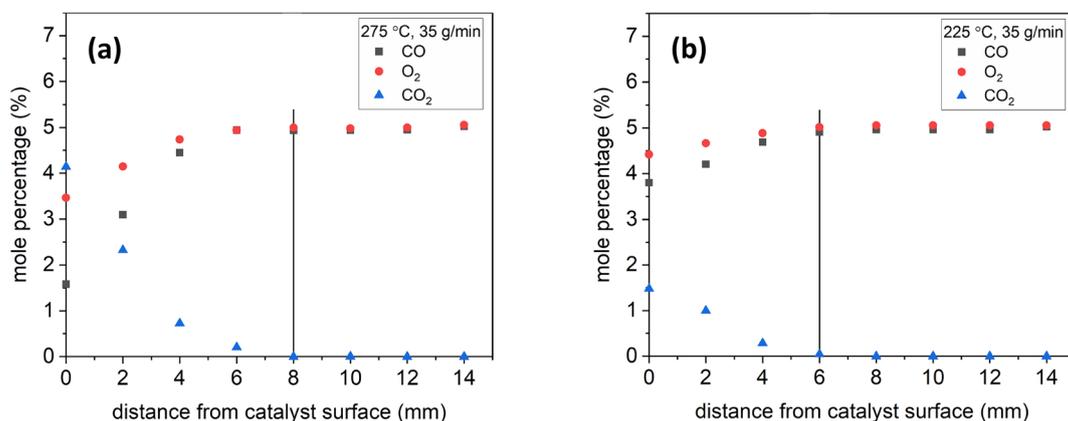

Fig. 7 Species profiles as a function of distance at 35 g min^{-1}, lean inlet composition, and 275 °C (a) & 225 °C (b). The vertical lines show where the CO_2 near-zero levels were reached away from the surface.

the mechanisms generated by Mhadeshwar and Vlachos,[23] Maestri et al.,[22] and Karakaya et al.,[19,24] the sticking coefficient for O_2 ranges from 0.01 to 0.05, whereas that of CO is around 0.5. Given the much lower sticking coefficient for O_2, more O_2 may be needed to compensate for the low adsorption of O_2, which is more pertinent at sufficiently high flowrates.

Reaction order, hysteresis behavior, and the water-gas shift reaction

To determine the reaction order with respect to CO, we changed the CO:O_2 volume ratio from 0.4 to 4 by fixing the

Table 3 CO conversion levels (%) as a function of temperature, flowrate and inlet composition

Temperature (°C)	35 g min^{-1}		24 g min^{-1}	
	Lean	Stoichiometric	Lean	Stoichiometric
275	68	68	75	85
250	60	38	72	84
225	23	9	55	70
200	<5	<5	13	19
175	0	0	<5	<5

O_2 content and increasing that of CO at the expense of the inert at 300 °C and 24 g min^{-1} of total flow. Fig. 8(a) shows the mol% of O_2 consumed as a function of CO partial pressure. Fig. 8(b) shows that below the stoichiometric ratio of 2, the order is positive. Beyond the stoichiometric ratio, the order is negative, indicating an inhibition effect.

Similarly, to determine the reaction order with respect to O_2, we changed the O_2:CO volume ratio from 0.4 to 4.0 by fixing the CO content and increasing that of O_2 at the expense of the inert at 300 °C and 24 g min^{-1} of total flow. Fig. 9(a) shows the mol% of CO consumed as a function of the partial pressure of O_2. Three kinetic regimes are observed (Fig. 9(b)). Below the stoichiometric ratio of 0.5, the order is positive. Beyond the stoichiometric ratio, a second regime exists in which the order is negative, indicating that increasing the partial pressure of O_2 beyond the stoichiometric ratio inhibits the CO oxidation. At higher partial pressures of O_2, a lower, negative order is observed, where the effect of O_2 is inhibiting but to a lesser extent.

Lee et al.[49] studied the low-temperature oxidation of methane on Pt, Pd and Ag–Pd catalysts, where they also observed three kinetic regimes: a positive order with respect
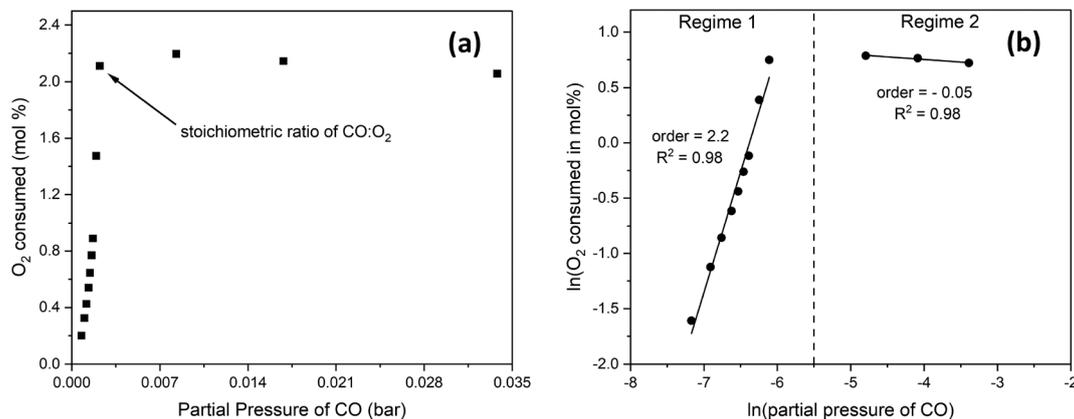
2504 | React. Chem. Eng., 2022, **7**, 2497–2507

This journal is © The Royal Society of Chemistry 2022

Fig. 8 (a) the mol% of O_2 consumed as a function of CO partial pressure at 300 °C and 24 g min^{-1}, with (b) showing the natural logarithm values where reaction orders can be extracted.

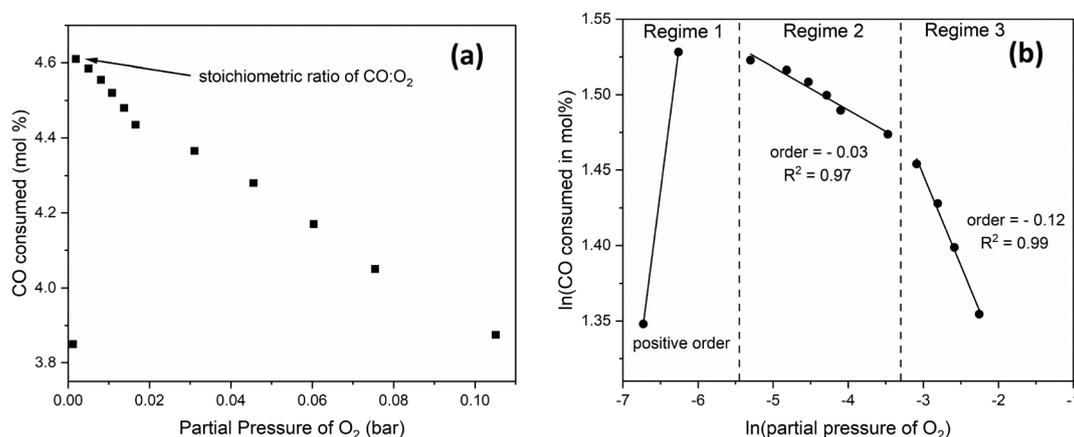**Fig. 9** (a) the mol% of CO consumed as a function of O_2 partial pressure at 300 °C and 24 g min^{-1}, with (b) showing the natural logarithm values where reaction orders can be extracted.

to O_2 below the stoichiometric ratio then decreasing orders as the partial pressure of O_2 increased. Using *in situ* X-ray absorption spectroscopy (XAS) and X-ray photoelectron spectroscopy (XPS), they attributed the reduction in catalyst activity at high O_2 partial pressure to the oxidation of the metals. While their study was on methane oxidation on Pt, Pd, and Ag–Pd catalysts, we expect Rh to behave similarly under CO oxidation conditions. Therefore, we propose that as the O_2 content increased, Rh was oxidized, resulting in lower activity. Additionally, Lee *et al.*[49] observed hysteresis as they decreased the partial pressure of O_2, and they attributed the observed bistability to the reduction of the metal by methane at decreasing partial pressures of O_2.

To investigate whether hysteresis would occur on Rh under CO oxidation conditions, we performed a hysteresis study, where after increasing the partial pressure of O_2 at the expense of the inert as shown in Fig. 9(a), we decreased the O_2 content back to the starting point. Hysteresis was indeed observed, shown in Fig. 10 in terms of steady-state CO conversion as a function of O_2:CO volume ratio. As the O_2 content decreased, CO reduced RhO$_x$, restoring the activity of the catalyst. Upon decreasing the O_2 content, the catalyst showed lower activity at

the same ratio compared to when increasing the O_2 content. The difference in reactivity between the two routes was lower as the stoichiometric ratio was approached, at which point bistability was no longer observed.
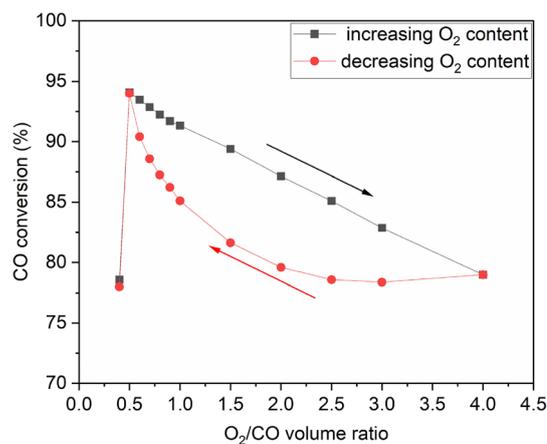

Fig. 10 Hysteresis observed when changing the O_2 content at the expense of the inert at 300 °C and 24 g min^{-1}.

This journal is © The Royal Society of Chemistry 2022

React. Chem. Eng., 2022, **7**, 2497–2507 | **2505**

A few theories have been developed to explain the irregularities of CO oxidation, such as bistability, on platinum group metals (PGM). The theories include effects of surface coverage, formation of metal oxides, formation of sub-surface oxygen during the reaction, and changes to the surface by the adsorbates.[50–53] In particular, hysteresis during low-temperature oxidation reactions of hydrocarbons on PGM catalysts is a common phenomenon, the extent of which depends on the oxophilicity of the catalyst and the reduction ability of the hydrocarbon.[54]

No hysteresis was observed when changing the $CO:O_2$ ratio by increasing and decreasing the CO content at the expense of the inert (Fig. S6†). This signifies no change in the oxidation state of the catalyst by the presence of CO. No hysteresis was observed when changing the temperature from 200 °C to 300 °C and back to 200 °C (Fig. S7†) either, which indicates no sintering of the catalyst upon short-time exposure to 300 °C. As for the water-gas shift reaction, we observed no reactivity in the temperature range studied, which is supported by previous literature reports.[55–57] Similarly, the addition of H_2O had no influence on the oxidation of CO in the temperature range studied, irrespective of inlet composition.

Conclusions

In this study we investigated Rh-catalyzed CO oxidation and WGS reaction in a stagnation-flow reactor. The catalyst characterization techniques show a change of the Al_2O_3 phase from γ to δ upon calcination in air at 700 °C for 2 hours, but the BET surface area and BJH pore volume remained similar to those typically found in the literature for Rh/Al_2O_3. Calcination did cause some Rh to be strongly bound to the surface, but H_2-TPR shows that easily accessible Rh, reducible at 160 °C, was still present. STEM and EELS images show the morphology of the reduced catalyst, with an average particle size of 5 nm, which corroborates the H_2-chemisorption results.

The stagnation-flow reactor experimental results show how the pressure, flowrate, temperature, inlet composition, and presence of H_2O affected reactivity. At 24 g min^{-1} of total flow, as we increased the temperature from 175 to 275 °C, the CO conversion increased from less than 5% to 75% and to 85% under lean and stoichiometric inlet compositions, respectively. The lower reactivity under lean conditions is attributed to O_2 occupying active sites at the expense of CO. At 35 g min^{-1} of total flow, there was a preference for the lean inlet composition at temperatures below 250 °C, due to CO surface coverage inhibiting the adsorption of O_2, which is compensated for by running lean. Investigating the reaction order with respect to O_2 revealed three kinetic regimes where the reaction order with respect to O_2 is positive below the stoichiometric ratio and negative with decreasing orders at increasing O_2 partial pressures. The reaction order with respect to CO is positive below the stoichiometric ratio, at which point the reaction order with respect to CO becomes negative. Lastly, we observed catalyst bistability as we increased and decreased the O_2 content at the expense of the inert, and we attribute that to the oxidation of the metal at sufficiently high O_2 content and the reduction of the metal by CO at decreasing O_2 content. We observed no hysteresis behavior while changing the CO content or the temperature, and we observed no water-gas shift reactivity over the temperature range tested. The current, thorough investigation aids in kinetic modeling of CO oxidation on Rh over a wide range of conditions, where accurate reaction rates can be obtained.

Conflicts of interest

There are no conflicts to declare.

Acknowledgements

References

1 *Air pollution: The silent killer that claims 7 million lives each year*, retrieved from **https://www.ohchr.org**, 2019.
2 *National Emission Inventory*, retrieved from **https://www.epa.gov**, 2021.
3 *EPA's Report on the Environment (ROE)*, 2021.
4 *World Energy Outlook*, 2021.
5 C. L. Feng, X. L. Liu, T. Y. Zhu and M. K. Tian, *Environ. Sci. Pollut. Res.*, 2021, **28**, 24847–24871.
6 S. Dey and G. C. Dhal, *Polytechnica*, 2020, **3**, 26–42.
7 G. C. Koltsakis and A. M. Stamatelos, *Prog. Energy Combust. Sci.*, 1997, **23**, 1–39.
8 H. Shinjoh, *Catal. Surv. Asia*, 2009, **13**, 184–190.
9 R. Kissel-Osterrieder, F. Behrendt, J. Warnatz, U. Metka, H. R. Volpp and J. Wolfrum, *Proc. Combust. Inst.*, 2000, **28**, 1341–1348.
10 A. D. Allian, K. Takanabe, K. L. Fujdala, X. Hao, T. J. Truex, J. Cai, C. Buda, M. Neurock and E. Iglesia, *J. Am. Chem. Soc.*, 2011, **133**, 4498–4517.
11 P. Aghalayam, Y. K. Park and D. G. Vlachos, *Proc. Combust. Inst.*, 2000, **28**, 1331–1339.
12 A. B. Mhadeshwar and D. G. Vlachos, *J. Phys. Chem. B*, 2004, **108**, 15246–15258.
13 A. B. Mhadeshwar and D. G. Vlachos, *Combust. Flame*, 2005, **142**, 289–298.
14 S. Raimondeau and D. G. Vlachos, *Comput. Chem. Eng.*, 2002, **26**, 965–980.

2506 | *React. Chem. Eng.*, 2022, **7**, 2497–2507

This journal is © The Royal Society of Chemistry 2022

15 A. V. Kalinkin, A. V. Pashis and V. I. Bukhtiyarov, *Kinet. Catal.*, 2007, **48**, 298–304.

16 T. Bunluesin, H. Cordatos and R. J. Gorte, *J. Catal.*, 1995, **157**, 222–226.

17 A. B. Mhadeshwar and D. G. Vlachos, *J. Catal.*, 2005, **234**, 48–63.

18 D. Shimokuri, H. Murakami, S. Hinokuma, Y. Matsumoto, S. Naing, K. Naito, H. Yokohata, H. Takebayashi and A. Miyoshi, *Combust. Sci. Technol.*, 2021, **193**, 2137–2157.

19 H. Karadeniz, C. Karakaya, S. Tischer and O. Deutschmann, *Chem. Eng. Sci.*, 2013, **104**, 899–907.

20 Y. P. Cai, H. G. Stenger and C. E. Lyman, *J. Catal.*, 1996, **161**, 123–131.

21 M. J. P. Hopstaken and J. W. Niemantsverdriet, *J. Chem. Phys.*, 2000, **113**, 5457–5465.

22 M. Maestri, D. G. Vlachos, A. Beretta, G. Groppi and E. Rronconi, *AIChE J.*, 2009, **55**, 993–1008.

23 A. B. Mhadeshwar and D. G. Vlachos, *J. Phys. Chem. B*, 2005, **109**, 16819–16835.

24 C. Karakaya, *PhD*, Karlsruher Institut für Technologie (KIT), 2012.

25 T. Yuan, Y. H. Lai and C. K. Chang, *Combust. Flame*, 2008, **154**, 557–568.

26 R. W. Sidwell, H. Y. Zhu, R. J. Kee, D. T. Wickham, C. Schell and G. S. Jackson, *Proc. Combust. Inst.*, 2002, **29**, 1013–1020.

27 R. J. Kee, M. E. Coltrin and P. Glarborg, *Chemically reacting flow: theory and practice*, Wiley-Interscience, Hoboken, NJ, 2003.

28 O. Deutschmann, L. I. Maier, U. Riedel, A. H. Stroemman and R. W. Dibble, *Catal. Today*, 2000, **59**, 141–150.

29 Y. K. Park, N. E. Fernandes and D. G. Vlachos, *Chem. Eng. Sci.*, 1999, **54**, 3635–3642.

30 G. Veser, M. Ziauddin and L. D. Schmidt, *Catal. Today*, 1999, **47**, 219–228.

31 S. H. Oh and C. C. Eickel, *J. Catal.*, 1991, **128**, 526–536.

32 J. M. Gatica, R. T. Baker, P. Fornasiero, S. Bernal, G. Blanco and J. Kaspar, *J. Phys. Chem. B*, 2000, **104**, 4667–4672.

33 S. Fuentes and F. Figueras, *J. Catal.*, 1980, **61**, 443–453.

34 D. W. Senser, J. S. Morse and V. A. Cundy, *Rev. Sci. Instrum.*, 1985, **56**, 1279–1284.

35 A. D. Abid, J. Camacho, D. A. Sheen and H. Wang, *Energy Fuels*, 2009, **23**, 4286–4294.

36 B. H. Zhao, R. Ran, Y. D. Cao, X. D. Wu, D. Weng, J. Fan and X. Y. Wu, *Appl. Surf. Sci.*, 2014, **308**, 230–236.

37 E. Diaz, J. A. Casas, A. F. Mohedano, L. Calvo, M. A. Gilarranz and J. J. Rodriguez, *Ind. Eng. Chem. Res.*, 2008, **47**, 3840–3846.

38 P. Osorio-Vargas, C. H. Campos, R. M. Navarro, J. L. G. Fierro and P. Reyes, *Appl. Catal., A*, 2015, **505**, 159–172.

39 R. Buchel, A. Baiker and S. E. Pratsinis, *Appl. Catal., A*, 2014, **477**, 93–101.

40 M. Bilal and S. D. Jackson, *Appl. Catal., A*, 2017, **529**, 98–107.

41 A. Boumaza, L. Favaro, J. Ledion, G. Sattonnay, J. B. Brubach, P. Berthet, A. M. Huntz, P. Roy and R. Tetot, *J. Solid State Chem.*, 2009, **182**, 1171–1176.

42 J. C. Vis, H. F. J. Vantblik, T. Huizinga, J. Vangrondelle and R. Prins, *J. Mol. Catal.*, 1984, **25**, 367–378.

43 M. Ojeda, M. L. Granados, S. Rojas, P. Terreros, F. J. Garcia-Garcia and J. L. G. Fierro, *Appl. Catal., A*, 2004, **261**, 47–55.

44 S. S. Kim, S. J. Lee and S. C. Hong, *Chem. Eng. J.*, 2011, **169**, 173–179.

45 J. M. Li, F. Y. Huang, W. Z. Weng, X. Q. Pei, C. R. Luo, H. Q. Lin, C. J. Huang and H. L. Wan, *Catal. Today*, 2008, **131**, 179–187.

46 R. Burch, P. K. Loader and N. A. Cruise, *Appl. Catal., A*, 1996, **147**, 375–394.

47 C. S. Gopinath and F. Zaera, *J. Catal.*, 2001, **200**, 270–287.

48 C. T. Campbell and J. M. White, *J. Catal.*, 1978, **54**, 289–302.

49 G. Lee, W. Q. Zheng, K. A. Goulas, I. C. Lee and D. G. Vlachos, *Ind. Eng. Chem. Res.*, 2019, **58**, 17718–17726.

50 E. A. Lashina, N. A. Chumakova, G. A. Chumakov and A. I. Boronin, *Chem. Eng. J.*, 2009, **154**, 82–87.

51 E. I. Latkin, V. I. Elokhin and V. V. Gorodetskii, *J. Mol. Catal. A: Chem.*, 2001, **166**, 23–30.

52 K. Krischer, M. Eiswirth and G. Ertl, *J. Chem. Phys.*, 1992, **96**, 9161–9172.

53 M. Eiswirth, K. Krischer and G. Ertl, *Surf. Sci.*, 1988, **202**, 565–591.

54 G. Lee, W. Q. Zheng, I. C. Lee and D. G. Vlachos, *Appl. Catal., A*, 2019, **587**.

55 G. G. Olympiou, C. M. Kalamaras, C. D. Zeinalipour-Yazdi and A. M. Efstathiou, *Catal. Today*, 2007, **127**, 304–318.

56 A. Donazzi, A. Beretta, G. Groppi and P. Forzatti, *J. Catal.*, 2008, **255**, 241–258.

57 C. Karakaya, R. Otterstatter, L. Maier and O. Deutschmann, *Appl. Catal., A*, 2014, **470**, 31–44.

This journal is © The Royal Society of Chemistry 2022

React. Chem. Eng., 2022, **7**, 2497–2507 | **2507**